Automated Non-Invasive Measurement of Single Sperm's Motility and Morphology

Changsheng Dai, Zhuoran Zhang, James Huang, Xian Wang, Changhai Ru, Huayan Pu, Shaorong Xie, Junyan Zhang, Sergey Moskovtsev, Clifford Librach, Keith Jarvi, and Yu Sun

***Abstract*— Measuring cell motility and morphology is important for revealing their functional characteristics. This paper presents automation techniques that enable automated, non-invasive measurement of motility and morphology parameters of single sperm. Compared to the status quo of qualitative estimation of single sperm's motility and morphology manually, the automation techniques provide quantitative data for embryologists to select a single sperm for intracytoplasmic sperm injection. An adapted joint probabilistic data association filter was used for multi-sperm tracking and tackled challenges of identifying sperms that intersect or have small spatial distances. Since the standard differential interference contrast (DIC) imaging method has side illumination effect which causes inherent inhomogeneous image intensity and poses difficulties for accurate sperm morphology measurement, we integrated total variation norm into the quadratic cost function method, which together effectively removed inhomogeneous image intensity and retained sperm's subcellular structures after DIC image reconstruction. In order to relocate the same sperm of interest identified under low magnification after switching to high magnification, coordinate transformation was conducted to handle the changes in the field of view caused by magnification switch. The sperm's position after magnification switch was accurately predicted by accounting for the sperm's swimming motion during magnification switch. Experimental results demonstrated an accuracy of 95.6% in sperm motility measurement and an error <10% in morphology measurement.**

***Index Terms*— Cell tracking, sperm motility, sperm morphology, automated measurement.**

Manuscript received February 6, 2018; revised May 17, 2018; accepted May 20, 2018. Date of publication May 25, 2018; date of current version October 1, 2018. This work was supported in part by the Natural Sciences and Engineering Research Council of Canada through the Discovery Grant and the Tier I Canada Research Chair, in part by the University of Toronto via the Connaught Innovation Award, in part by the National Natural Science Foundation of China under Grants 61774107, 51575333, and 91748116, and in part by the Science and Technology Commission of Shanghai under Grant 16441909400. *(Changsheng Dai and Zhuoran Zhang contributed equally to this work.) (Corresponding author: Yu Sun.)*

C. Dai, Z. Zhang, J. Huang, X. Wang, and Y. Sun are with the Department of Mechanical and Industrial Engineering, University of Toronto, Toronto, ON M5S 3G8, Canada (e-mail: sun@mie.utoronto.ca).

C. Ru is with the Research Center of Robotics and Micro System, Soochow University, Suzhou 215021, China, and also with the Collaborative Innovation Center of Suzhou Nano Science and Technology, Soochow University, Suzhou 215021, China.

H. Pu and S. Xie are with the School of Mechatronic Engineering and Automation, Shanghai University, Shanghai 200072, China.

J. Zhang, S. Moskovtsev, and C. Librach are with the CReATe Fertility Centre, Toronto, ON M5S 1N8, Canada.

K. Jarvi is with the Mount Sinai Hospital, Toronto, ON M5G 1X5, Canada.

This paper has supplementary downloadable material available at http://ieeexplore.ieee.org, provided by the author.

Color versions of one or more of the figures in this paper are available online at http://ieeexplore.ieee.org.

Digital Object Identifier 10.1109/TMI.2018.2840827

I. Introduction

THE locomotive behaviors and shapes of cells reveal their functional characteristics, and measuring their motility and morphology parameters is required for both fundamental research and practical applications. Motility and morphology changes of bacteria and unicellular parasites reflect their virulence, and measuring these changes is useful for drug screening [1]. Measuring cancer cells' motility and morphology is important for investigating their migration and invasion mechanisms [2], [3] and for evaluating the efficacy of therapeutics [4]. In *in vitro* fertilization (IVF), motility and morphology of sperms indicate fertility potential [5], [6], and the measurement is prevalently used for infertility diagnosis and treatment. Intracytoplasmic sperm injection (ICSI), which is used in 70% of IVF treatments [7], involves the insertion of a single sperm into an oocyte by a micropipette. However, since the invention of ICSI in 1992, single sperm selection in ICSI has been qualitatively made by embryologists, who observe sperm motility and morphology and choose a sperm based on their experience [8], [9]. Automated, accurate, and non-invasive measurement of motility and morphology of single sperms can assist embryologists for quantitative sperm selection for ICSI use.

Fig. 1(a) summarizes the most important motility and morphology parameters of a sperm defined by the World Health Organization (WHO) [10]. Automated motility measurement is achieved by computer vision tracking sperms [11], and motility parameters are calculated based on the tracked trajectories. Among existing commonly used methods, the nearest neighbor (NN) method associates the nearest measurement to the tracked sperm, and the global nearest neighbor (GNN) method finds the best association between measurements and targets by minimizing the sum of pair-wise distances [12]. However, neither NN nor GNN accounts for the possibility of false association. Since a clinical sample has a high number of sperms, intersections and close proximity of sperms often cause mismatch of tracked sperms when the NN and GNN methods are used [13].

Automated morphology measurement of a sperm is performed by image segmentation of the sperm and its components such as the head and tail. To increase contrast, sperms are invasively fixed and stained so that the sperm can be easily identified and its different components segmented by color

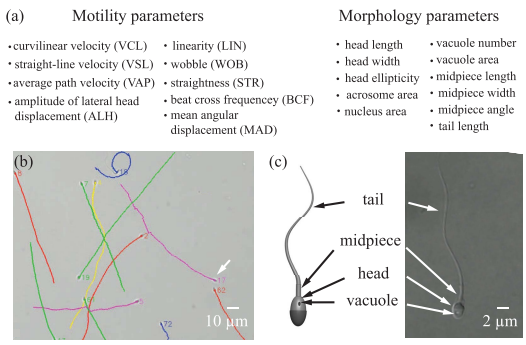

Fig. 1. (a) The motility and morphology parameters automatically measured on single sperms. (b) Multiple sperm tracking for motility measurement under low magnification (20×objective) with each sperm's trajectory marked. Arrow points to a sperm of interest. (c) The sperm of interest was automatically relocated in the field of view for morphology measurement after switching to high magnification (100×). The schematic and image show the anatomy of the sperm, with the head, midpiece, tail, and vacuole arrow labeled.

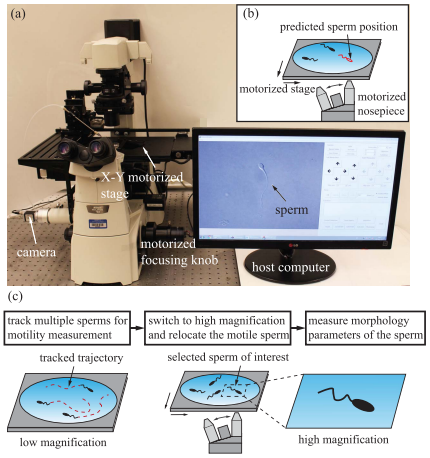

Fig. 2. (a) System for automated measurement of motility and morphology parameters of single sperms. (b) Right before magnification switch, the motile sperm's position after magnification switch is predicted, followed by automatic magnification switch and relocating the same sperm for morphology measurement. (c) Operation sequence of automated measurement of motility and morphology parameters for the same sperms.

differences [14], [15]. However, fixation and staining destroy the sperm and its DNA, making the sperm after measurement clinically unusable. Taking advantage of visualizing refractive index difference, differential interference contrast (DIC) imaging non-invasively increases the contrast of a sperm [16], and has been widely used by embryologists to examine sperm morphology prior to ICSI [17], [18]. The side illumination effect (i.e., bright on the one side and dark on the other side) in DIC images is instrumental for manual observation but poses difficulties to image processing due to image intensity inhomogeneity [19].

For a single sperm, non-invasively measuring both motility and morphology of the same sperm has yet to be achieved. The motility parameters are measured under a low magnification (such as 20× objective) to have a large field of view for obtaining sperms' trajectories [Fig. 1(b)]. The morphology parameters need to be measured under a high magnification to quantify subcellular structures. For instance, a motile sperm may have vacuoles on its head [Fig. 1(c)], the presence of which indicates DNA damage [20]. Using a sperm with vacuoles for IVF treatment can cause fertilization failure [21]. Since vacuoles are smaller than 1 μm, a high magnification objective (e.g., 100×) is often used [22]. Thus, measuring both motility and morphology of sperms requires switching between low and high magnifications.

However, switching to a high magnification significantly reduces the field of view (e.g., 25 times smaller from 20× to 100×), and sperm's fast movement (e.g., >20 μm/s) can make the motile sperm of interest identified under low magnification disappear under high magnification after switch. The previous attempt to keep track of the same object during magnification switch was implemented using motorized zoom, and the same object was kept in the field view by visual servoing [23]. However, this approach is not compatible with standard inverted microscopes, and its maximum imaging resolution of 1.4 μm is insufficient for visualizing subcellular structures such as vacuoles on sperm head. Automatically and non-invasively measuring motility and morphology of the same single sperm remains unsolved.

The problems tackled in this work include: (1) how to visually track individual sperms when they intersect with each other; (2) how to accurately relocate the same single sperm after switching to high magnification; and (3) how to accurately measure sperm morphology parameters under high-magnification DIC imaging. The system solved these challenges by integrating several techniques, including adapted joint probabilistic data association filtering for sperm tracking, coordinate transformation and position prediction of a motile sperm for relocating the same sperm after switching to high magnification, and DIC image reconstruction for non-invasive morphology measurement. Experimental results demonstrate that the system achieved an accuracy of 95.6% for multiple sperm tracking and motility measurement. The positioning accuracy for relocating the same sperm to the center of field of view after magnification switch is 5.2 μm. The errors for the measurement of all morphology parameters are within 10%.

II. System Setup

As shown in Fig. 2(a), the system was built around an inverted microscope equipped with an X-Y motorized stage and motorized control of the nosepiece and focusing. The motorized nosepiece contains a 20× objective (Nikon Plan Fluor) and a 100× objective (Nikon Plan Apo) among other objectives. A camera (acA1300-30gc, Basler) was connected to the microscope to capture images at 30 frames per second.

As summarized in Fig. 2(c), the system first performs automated sperm motility measurement under low magnification. Multiple sperms are simultaneously tracked and their trajectories are used to quantify all motility parameters [Fig. 1(b)]. Images in multiple fields of view are captured by moving the motorized X-Y stage. A motile sperm of interest is selected automatically or by a human operator via computer mouse clicking, and its position after magnification switch is

predicted. Then the system automatically switches to a high magnification objective and relocates the same sperm inside the field of view [Fig. 1(c)]. Under high magnification, automated non-invasive morphology measurement is conducted.

III. Key Methods

A. Motility Measurement Based on Sperm Tracking

For analyzing multiple sperms, the motility parameters of all sperms within a field of view need to be measured. As discussed earlier, sperm motility parameters are derived from the trajectory of each sperm (e.g., VCL, the time-average velocity of the sperm along its trajectory); therefore, it is essential to obtain the trajectories of individual sperms. Tracking multiple sperms in a clinical sample is challenging because sperms cross over each other and interference from proximal sperms is unavoidable. The measured position for a target sperm may not originate from the sperm but from another sperm in close proximity, causing uncertainty in data association. Among the methods for multiple object tracking, multiple hypothesis tracker (MHT) exploits the entire measurement history to estimate the state of each target but suffers rapidly growing memory with increasing time duration and the number of targets [24]. Instead of using the entire measurement history in MHT, joint probabilistic data association filter (JPDAF) [25] is advantageous for real-time multiple sperm tracking by only using the current measurement. To reduce data association uncertainty, JPDAF enumerates all association cases between targets and measurements and updates association probability.

Different from standard JPDAF which only uses the kinematics information (position and velocity) of the target for tracking, we adapted JPDAF by incorporating sperm shape information (head orientation) to further reduce data association uncertainty for robust multiple sperm tracking under interferences. The inclusion of head orientation was experimentally proven to significantly improve multi-sperm tracking and the quantification of motility parameters.

In the adapted JPDAF method, the state vector of a sperm at time (frame) k is

$$X_k = [x \ y \ \theta \ \dot{x} \ \dot{y} \ \dot{\theta}]^T \tag{1}$$

where (x, y) is the 2D position of the sperm head obtained by calculating the centroid of the sperm head contour, and θ is the angle between the major axis of the sperm head and the horizontal axis of the image plane. The inclusion of head orientation θ effectively reduces data association uncertainty in multiple sperm tracking. JPDAF calculates the Mahalanobis distance D_k between the predicted measurement $\tilde{Z}_k = [\tilde{x}, \tilde{y}, \tilde{\theta}]^T$ and the actual measurement $Z_k = [x, y, \theta]^T$ for data association, according to

$$D_k = \sqrt{(Z_k - \tilde{Z}_k)^T S^{-1} (Z_k - \tilde{Z}_k)} \tag{2}$$

where S is the innovation covariance matrix corresponding to the correct measurement. When two sperms intersect, the difference in their head orientations contributes to a larger Mahalanobis distance D_k and thus a smaller association probability, thereby reducing data association uncertainty.

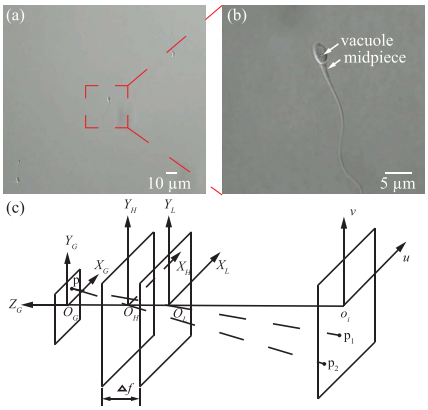

Fig. 3. (a) A sperm of interest under 20× magnification. (b) The same sperm under 100× magnification, and its subcellular structures such as vacuole and midpiece are clearly visible (arrow labeled). (c) Microscope model with objectives of different magnifications for coordinate transformation. Magnification switch from low to high changes the field of view and focus. O_G is the global coordinate system. O_H is the high magnification objective plane, and O_L is the low magnification objective plane. o_i is the image plane.

JPDAF updates the association probability between targets and measurements by enumerating all association cases α and accumulating the probability of each association case. The association probability $\beta_{jt}(k)$ that measurement j is associated to sperm t at time k is

$$\beta_{jt}(k) = \sum_{\alpha} P_k(\alpha) \omega_{jt}(\alpha, k) \tag{3}$$

where $P_k(\alpha)$ is the probability of association case α calculated from Mahalanobis distance D_k; $\omega_{jt}(\alpha, k)$ equals 1 if in association case α, measurement j is associated to sperm t, and equals 0 otherwise. This adapted JPDAF algorithm incorporates sperm head orientation into the state model and associates each sperm to the measurement based on the updated association probability $\beta_{jt}(k)$ in each image frame.

B. Automated Magnification Switch and Sperm Relocation

Visualization of subcellular structures of a sperms is necessary for morphology measurement, which requires the switching from 20× low magnification [Fig. 3(a)], after motility measurement, to 100× high magnification [Fig. 3(b)] to clearly reveal the vacuole and midpiece. Since magnification switch changes the field of view and the focus, in order to relocate the same sperm after magnification switch, coordinate transformation between different magnifications is used to relocate the sperm of interest inside the field of view and in focus after switching from low to high magnification. To compensate for the sperm's motion during magnification switch, the motile sperm's position after magnification switch is predicted.

Fig. 3(c) shows the microscope model with objectives of different magnifications for coordinate transformation. A point p in the global coordinate system (O_G) is projected through the low magnification objective plane (O_L) to point p_1 in the image plane (o_i). After magnification switch, the point p is projected through the high magnification objective plane (O_H)

to point p_2 in the image plane (o_i). Transformation in the image plane from the coordinate vector U_L under low magnification to the coordinate vector U_H under high magnification is

$$U_H = \begin{bmatrix} u_h \\ v_h \\ 1 \end{bmatrix} = KU_L = \begin{bmatrix} k_u & 0 & t_u \\ 0 & k_v & t_v \\ 0 & 0 & 1 \end{bmatrix} \begin{bmatrix} u_l \\ v_l \\ 1 \end{bmatrix} \tag{4}$$

where K is the transformation matrix from low magnification to high magnification; k_u and k_v are magnification factors along the u and v axes, respectively; t_u and t_v are translation factors along the u and v axes. Transformation matrix K is obtained using the least square method

$$K = \tilde{U}_H \tilde{U}_L^T (\tilde{U}_L \tilde{U}_L^T)^{-1} \tag{5}$$

where $\tilde{U}_L$ and $\tilde{U}_H$ are 3×N matrices containing N coordinate vectors under low and high magnifications, respectively.

To switch magnifications, the image coordinates of a sperm under the low magnification objective are transformed to the corresponding image coordinates under the high magnification objective. Then the motorized stage moves the sperm to the desired image coordinates under the high magnification objective. Besides changing the field of view, magnification switch also changes the focus of the sperm. The change of focus distance Δf was experimentally calibrated, and the motorized focusing knob is controlled to compensate for the change of focus distance after magnification switch.

Switching to a high magnification significantly reduces the field of view, and the sperm's swimming motion during microscope objective switch can cause the sperm to be out of the field of view after magnification switch. Therefore, the motile sperm's position after magnification switch is predicted to compensate for the sperm motion and keep the sperm inside the field of view after switching to high magnification [Fig. 2(b)]. Let Δt denote the time needed for switching from the low-magnification objective to the high-magnification objective. The sperm's position P after magnification switch is predicted as

$$P = \begin{bmatrix} x \\ y \end{bmatrix} = \begin{bmatrix} x_{prev} \\ y_{prev} \end{bmatrix} + \Delta t \cdot v \cdot \begin{bmatrix} \cos\theta \\ \sin\theta \end{bmatrix} \tag{6}$$

where (x, y) is the predicted position of the sperm head after magnification switch, and (x_{prev}, y_{prev}) is the sperm head's position measured before magnification switch; v and θ are the swimming velocity and head orientation of the sperm, respectively.

Based on coordinate transformation as well as the predicted sperm position under high magnification immediately after magnification switch, the system performs magnification switch and controls the motorized stage to relocate the target sperm under high magnification. Right after magnification switch, adapted JPDAF (as discussed in Section III.A) is initiated again to track the sperm, and the motorized stage is visually servoed to keep the motile sperm at the center of field of view under high magnification.

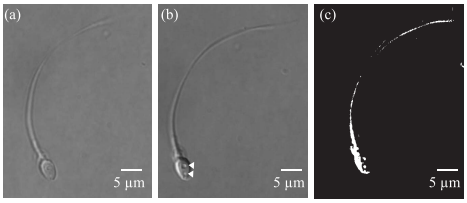

Fig. 4. The same sperm under 100× magnification: (a) bright-field; (b) DIC imaging. (a) The sperm is of low contrast under bright-field, and its subcellular structures are invisible. (b) DIC renders higher contrast, and two vacuoles (white triangles) are clearly seen on the sperm head. The side illumination effect of DIC makes the left side of the sperm brighter than its right side. (c) Binary image generated from thresholding the DIC image. Without image reconstruction, the left and right sides of the sperm are mistakenly divided into foreground and background, respectively.

C. Non-Invasive Morphology Measurement

Sperm morphology measurement requires visualizing the subcellular structures of a sperm, which are not visible under bright-field imaging due to sperms' low contrast [Fig. 4(a)]. For non-invasively enhancing sperm contrast, differential interference contrast (DIC) imaging is widely used [17], [18]. In DIC imaging, a light beam first passes through a polarizer so that the light waves oscillate only in one direction. Then the light beam is split by the condenser prism into two beams. These two light beams pass through the specimen and are compiled by the objective prism and the analyzer. The interference of the two light beams convert the invisible phase difference between them into the intensity variation [26].

A brightfield image of a sperm under 100× objective is shown in Fig. 4(a). The sperm is of low contrast, and its subcellular structures such as vacuoles on its head are hardly seen. In comparison, a DIC image [Fig. 4(b)] of the sperm reveals that DIC imaging renders higher contrast of the sperm, and two vacuoles are clearly seen on the sperm head. It can also be seen in the DIC image that the side illumination effect of DIC causes inhomogeneous image intensity, making the left side of the sperm appears brighter and the right side of the sperm darker. Due to this unique characteristic of DIC imaging, DIC image must be properly reconstructed before image segmentation to avoid wrongly segmenting the bright and dark sides of the sperm into different groups. If thresholding is applied to segment the DIC image, the left and right sides of the sperm would be mistakenly divided into foreground and background, respectively [Fig. 4(c)].

The purpose of DIC image reconstruction is to remove the inherent intensity inhomogeneity, for which reconstruction methods such as Hilbert transform and Wiener filtering have been developed [27]. Image smoothing is necessary in these methods to encourage nearby pixels to have the same reconstruction value. However, image smoothing also leads to the loss of subtle edge information, which is critical for reflecting the subcellular structures of a sperm. To preserve these subtle edges, we introduce total variation norm [28] into the cost function for DIC image reconstruction. By minimizing the total variation of the image subject to a close match to the original image, total variation norm smooths the image while well preserving the edges. The total variation norm D of

TABLE I
AUTOMATED MOTILITY AND MORPHOLOGY MEASUREMENT OF SINGLE SPERMS (AU: ARBITRARY UNIT)

	Motility									Morphology										
										Head			Acrosome	Nucleus	Vacuole		Midpiece			Tail
Sperm	VCL (μm/s)	VSL (μm/s)	VAP (μm/s)	ALH (μm/s)	LIN (AU)	WOB (AU)	STR (AU)	BCF (Hz)	MAD (°)	length (μm)	width (μm)	ellipticity (AU)	area (μm^2)	area (μm^2)	number (AU)	area (μm^2)	length (μm)	width (μm)	angle (°)	length (μm)
1	12.40	12.13	12.53	0.10	0.98	1.01	0.97	12.18	0.15	5.69	3.02	1.88	4.25	9.26	2	1.32	5.18	0.94	7.03	41.11
2	3.12	1.54	2.71	0.06	0.49	0.87	0.57	13.20	0.74	5.90	2.88	2.05	7.13	6.22	1	0.61	4.90	1.01	21.4	37.66
3	7.90	7.24	7.92	0.10	0.92	1.00	0.91	9.14	0.22	5.83	3.24	1.8	6.82	8.02	1	1.17	4.82	0.86	8.80	40.54
4	15.33	15.00	15.24	0.16	0.98	0.99	0.98	9.65	0.13	6.05	3.17	1.91	5.45	9.60	0	NA	4.90	0.86	5.00	39.60
5	15.60	15.48	15.68	0.11	0.99	1.01	0.99	12.69	0.11	5.69	3.38	1.68	5.94	9.18	0	NA	4.82	1.01	1.76	37.58

image f is

$$D(f) = \sum \sqrt{|\bigtriangledown f|^2} = \sum_{x,y} \sqrt{(\partial_x f)^2 + (\partial_y f)^2} \tag{7}$$

where $\bigtriangledown f$ is the gradient of f; ∂_x and ∂_y are difference operators along the x and y axes, respectively; and $\partial_x f = f(x+1, y) - f(x, y)$, $\partial_y f = f(x, y+1) - f(x, y)$.

DIC image g is modeled as the convolution of the point spread function (PSF) of DIC imaging with the expected reconstructed image f. The PSF of DIC is approximated as Gaussian derivative d_λ along the DIC side illumination direction λ [16],

$$g = d_\lambda * f \tag{8}$$

Image reconstruction from DIC imaging is achieved by minimizing the quadratic cost function

$$O(f) = \int E \mathrm{d}\lambda = \int [(d_\lambda * f - g)^2 + w_s (k * f)^2 + w_r f^2] \mathrm{d}\lambda \tag{9}$$

where w_s and w_r are the weights for smoothing and regularity terms; and k is the smoothing operator and is adapted to be the total variation norm in (8) for preserving edges. The reconstructed image f that minimizes (9) is obtained by solving the Euler-Lagrange equation [29]

$$\frac{\partial E}{\partial f} - \frac{\partial}{\partial \lambda} \frac{\partial E}{\partial f_\lambda} = 0 \tag{10}$$

Substituting (9) into (10) gives

$$-d_\lambda * (d_\lambda * f - g) + w_s \cdot k * k * f + w_r \cdot f = 0 \tag{11}$$

From (11), the reconstructed image f is obtained.

After DIC image reconstruction, image segmentation is performed using fuzzy c-means clustering incorporated with spatial information [30]. Fuzzy c-means clustering achieves soft segmentation by using the partial membership function borrowed from the fuzzy set theory to allow a pixel to belong to more than one clusters. In contrast to hard segmentation by partitioning each pixel exclusively to one cluster, fuzzy c-means clustering is more effective in dealing with low-contrast objects and intensity variations of the image background [31]. The incorporated spatial information helps segment the pixels with similar intensity but spatially far away from each other. The different components (head, midpiece and tail) of the sperm are automatically detected based on the distance differences of each component's contour to the skeleton of the sperm [32].

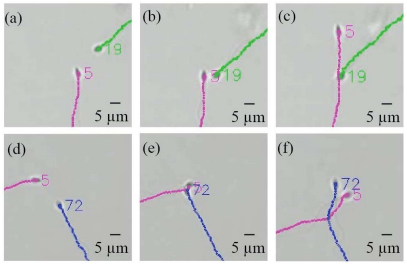

Fig. 5. (a)(b)(c) show the tracking of two sperms in close proximity. (d)(e)(f) show the tracking of two sperms in intersection.

IV. EXPERIMENTAL RESULTS AND DISCUSSION

Human sperm used in experiments were obtained from CReATe Fertility Centre (Toronto) and informed consent was obtained from all subjects. The medium contained modified human tubal fluid mixed with 7% PVP (polyvinylpyrrolidone, Irvine Scientific), as used in clinical ICSI.

A. Sperm Tracking and Motility Measurement

Our system automatically measured the WHO-stipulated motility parameters, including VCL, VSL, VAP, ALH, LIN, WOB, STR, BCF, MAD (as summarized in Table I, see Fig. 1(a) for acronym definition), via multiple sperm tracking. To evaluate the performance of multiple sperm tracking, we used the MOTA metric [33], which is a standard metric for evaluating multiple object tracking algorithms. Tracking accuracy (MOTA) is defined as

$$\mathrm{MOTA} = 1 - \frac{\mathrm{n_{miss}} + \mathrm{n_{false\_positive}} + \mathrm{n_{mismatch}}}{\mathrm{n_{total}}}$$

where $\mathrm{n_{miss}}$ is the number of targets missed during tracking; $\mathrm{n_{false\_positive}}$ is the number of misidentified targets; $\mathrm{n_{mismatch}}$ is the number of mismatched targets due to close proximity and intersections; and $\mathrm{n_{total}}$ is the total number of targets.

Tracking multiple sperms requires correctly identifying each sperm including those that are in close proximity and crossing over each other. Compared to the standard JPDAF algorithm, our adapted JPDAF algorithm incorporates the additional information of sperm head orientation in (1) to reduce data association uncertainty. Fig. 5(a)(b)(c) show the successful

TABLE II
PERFORMANCE OF MULTIPLE SPERM TRACKING
(S:STANDARD JPDAF, A: ADAPTED JPDAF)

Sample	1		2		3		4		5	
Method	S	A	S	A	S	A	S	A	S	A
Frames	540		600		510		570		540	
n_{total}	33		39		27		45		36	
n_{miss}	2	2	1	1	1	1	1	1	1	1
$n_{false\_positive}$	0	0	0	0	0	0	0	0	0	0
$n_{mismatch}$	4	0	6	0	4	0	8	2	6	0
MOTA (%)	81.8	93.9	82.1	97.4	81.5	96.3	80.0	93.3	80.6	97.2

tracking of two sperms before, during and after close proximity, and Fig. 5(d)(e)(f) show the successful tracking of two sperms before, during and after intersection. These are challenging scenarios for the standard JPDAF algorithm that does not consider sperm head orientation differences. Quantitative comparison of standard JPDAF and our adapted JPDAF algorithms in terms of MOTA value confirmed the advantage of our adapted method (n=2,760 frames of images; average MOTA value: 81.2% achieved by standard JPDAF vs. 95.6% achieved by adapted JPDAF), as summarized in Table II.

The missing of sperms (n_{miss} in Table II) was caused by sperms swimming out of the focal plane. Multiple sperms were tracked within a field of view, and our system was designed not to perform auto-focusing for continuing to track a sperm when it swims out of the focal plane and becomes out-of-focus. The mismatch of two sperms ($n_{mismatch}$ in Sample 4) using adapted JPDAF was due to rare events where two sperms intersect not only in the XY plane but also in the Z direction. In this case, two sperms physically attached to each other (see Supplementary Video), causing mismatch in tracking.

B. Automated Magnification Switch and Sperm Relocation

After sperm tracking for motility measurement, the system performed automated magnification switch to relocate the single sperm that was specified under low magnification to the center of the field of view under high magnification. Relocating the sperm after magnification switch was achieved by coordinate transformation and sperm position prediction. Coordinate transformation was calibrated using a commercial calibration grid slide. The positions of twenty points on the calibration grid were recorded under both low magnification (20×) and high magnification (100×). The transformation matrix in (4) was obtained using the least squares method (5), and the calibration results are summarized in Table III.

Experiments were performed to evaluate the positioning accuracy of coordinate transformation for relocating the same object to the center of field of view after magnification switch. A total of 40 points on the calibration slide were selected under low magnification, with the shortest distance of 18.3 μm to the center of field of view and the largest distance of 171.2 μm (size of field of view under 20×: 432 μm×324 μm). Each point was automatically relocated after switching to high magnification. The distance of a target point to the center of the field of view under high magnification

TABLE III
CALIBRATION RESULTS FOR MAGNIFICATION SWITCH

Parameters	20× to 100×	100× to 20×
k_u	5.0	0.2
k_v	5.0	0.2
t_u (pixel)	-3070.5	617.3
t_v (pixel)	-3007.6	609.1
Δf (μm)	45	-45

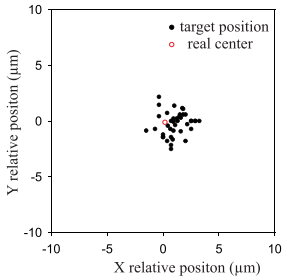

Fig. 6. Forty target points selected under 20× were relocated under 100× after magnification switch.

was measured as the positioning accuracy for relocation. Fig. 6 shows the positions of the 40 target points relocated after magnification switch relative to the center of field of view. The positioning accuracy for relocation was 1.7±0.6 μm (n=40). The error was caused by the microscope model [Fig. 3(c)] that does not take into account out-of-plane rotation of the objective planes relative to the image plane. The out-of-plane rotation arises from the structural design of standard motorized nosepieces and the fixation of objectives in optical microscopes. The positioning error of 1.7±0.6 μm, however, is negligible for the purpose of successfully relocating a sperm after magnification switch since the size of the field of view under 100×objective is approximately 86 μm×65 μm and the total length of a sperm is around 50 μm.

The performance of relocating the same motile sperm was then evaluated. Fifty sperms were selected sequentially under 20× for relocation under under 100×. The time for the microscope to complete the switch of objectives [Δt in (6)] costs 2 seconds, which includes lowering the low magnification objective, switching to high magnification objective, and raising the high magnification objective. A sperm was first tracked and centered in the field of view before magnification switch. According to (6), its motion during magnification switch was compensated for, and its position after magnification switch was predicted to keep the sperm within the field of view after magnification switch. For each sperm, after magnification switch and relocating the sperms, the distance of the sperm to the center of the field of view under 100× was measured. For the fifty sperms, the positioning accuracy for relocation was 5.2±2.6 μm. While the value of v in (6) was set to be the average velocity determined in sperm tracking under 20× and θ was set to be the head orientation measured immediately before magnification switch, the velocity and head orientation of a motile sperm both change over time. Therefore, the accuracy of relocating sperms was lower than

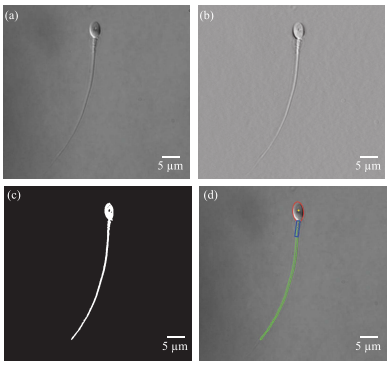

Fig. 7. (a) DIC image of a sperm under 100× magnification. (b) Reconstructed image of the sperm from DIC imaging. (c) The sperm is segmented from the reconstructed image using fuzzy c-means clustering. (d) Different parts (the head including a vacuole, midpiece, and tail) of the sperm are detected with respective contour labeled on the image.

that of relocating target points on the calibration grid slide (5.2±2.6 μm vs. 1.7±0.6 μm).

C. Non-Invasive Morphology Measurement

The side illumination effect of DIC imaging causes inherent inhomogeneity of image intensity. As seen in Fig. 7(a), the left side of the sperm is brighter than the right side. Fig. 7(b) shows the image reconstructed according to (9), where the side illumination effect of DIC imaging was largely removed. Due to our use of total variation norm (7), the edges of the sperm especially those of the subcellular structures were preserved after DIC image reconstruction.

Fig. 7(c) shows the sperm segmented from the background by fuzzy c-means clustering. Notably, a hole exist in the head of the segmented sperm, indicating the presence of a vacuole on the sperm head. The different components (head, midpiece and tail) of the sperm were also detected [Fig. 7(d)]. Morphology parameters were then measured on each component of the sperm, as summarized in Table I where Sperm 3 corresponds to the sperm shown in Fig. 7. The iteration of fuzzy c-means clustering ended when the change of the membership function between two successive iterations was less than the threshold of 0.02. The threshold value was tuned experimentally by accounting for the tradeoff between segmentation accuracy and required computation time. The time cost for automated morphology measurement of a sperm, including DIC image reconstruction, image segmentation and parameter measurement, was 0.35 second (Intel i7 processor, 3.4 GHz).

Experiments were conducted on 50 sperms to evaluate the accuracy of morphology measurement. The results from automated morphology measurement were compared with those by manual benchmarking using zoomed-in images in ImageJ with best care. The errors of automated measurement for different morphology parameters are summarized in Fig. 8 (n=50). The error (±standard error of mean) for measuring sperm head length was 3.7±0.3%, for head width was 4.6±0.4%, for acrosome area was 5.1±0.3%, for nucleus area was 7.0±0.4%, for vacuole area was 8.1±0.5%, for midpiece length was 9.6±0.5%, for midpiece width was 7.3±0.3%, for midpiece angle was 8.5±0.4%, for tail length was 9.0±0.6%. The measurement errors for all morphology parameters were <10%, which are acceptable for determining normal sperms [32]. One source of these errors was due to heterogeneity of sperms [34]. For instance, although most sperms have clearly different widths in their midpieces and tails, such difference in a low number of sperms is small (see Supplementary Video). Hence, the threshold value set for segmenting the midpiece and tail in our system was effective in distinguishing this difference in the vast majority but not all of the sperms tested. Excess cytoplasm residual at the sperm neck, which occurred in a few cases, also impeded properly segmenting sperm head and midpiece.

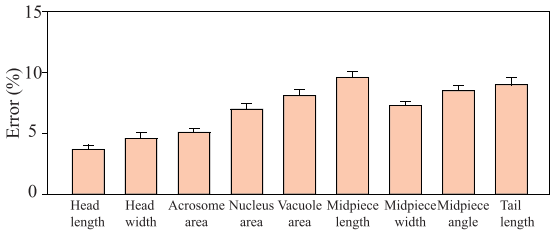

Fig. 8. Errors of automated morphology measurement compared to manual benchmarking. n=50.

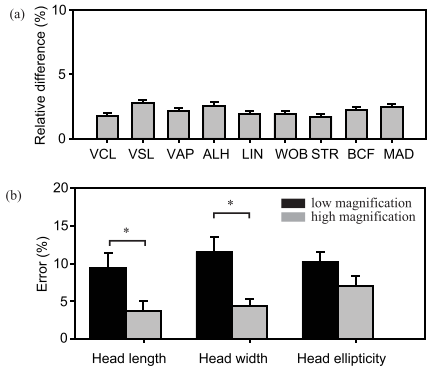

Fig. 9. (a) Relative difference of motility parameters measured under low and high magnifications. (b) Errors of head length, head width, and head ellipticity measured under low and high magnifications. The difference for head length and head width measured under low and high magnifications is significant ($p < 0.05$). n=50.

We also investigated the difference of motility measurements under low and high magnifications. The relative differences of the 9 motility parameters measured under low magnification and under high magnification are summarized in Fig. 9(a). The difference for each of the 9 motility parameters was within 5%. However, for morphology measurement, due to the lower imaging resolution under low magnification (20× vs. 100×), only three morphology parameters (i.e., head length, head width, and head ellipticity) were compared while other morphology parameters can only be measured under 100×. As summarized in Fig. 9(b), for each of the three morphology parameters, accuracy of measurements made under high magnification is higher than under low magnification.

Fig. 10 shows the distribution of motility and morphology parameters from 50 sperms of one patient sample, quantitatively revealing the heterogeneity of sperms from

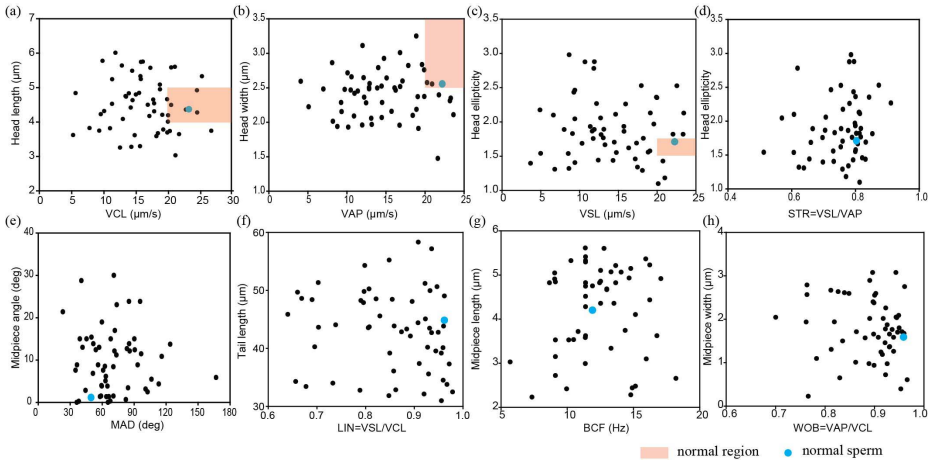

Fig. 10. Distribution of 50 sperms' motility and morphology parameters. (a) head length vs. VCL. (b) head width vs. VAP. (c) head ellipticity vs. VSL. (d) head ellipticity vs. STR. (e) midpiece angle vs. MAD. (f) tail length vs. LIN. (g) midpiece length vs. BCF. (h) midpiece width vs. WOB. The highlighted regions in (a)(b)(c) were resulted from applying WHO-stipulated criteria that define a normal sperm. The only sperm that satisfies the criteria is labeled as an enlarged dot.

the same population. According to the criteria stipulated by WHO, normal sperms should have swimming velocity higher than 20 μm/s, head length between 4 and 5 μm, head width between 2.5 and 3.5 μm, and head ellipticity between 1.5 and 1.75 [35], [36]. Applying these criteria identifies the highlighted regions in Fig. 10(a)(b)(c) where the horizontal and vertical axes are sperms' swimming velocity (VCL, VAP, VSL) and head morphology parameters, respectively. Only one sperm (labeled as enlarged dot) out of the 50 sperms satisfied the WHO-stipulated criteria. In clinical practice, the selected sperm is aspirated into a standard micropipette [11] for ICSI use. For other motility and morphology parameters of the 50 sperms shown in Fig. 10(d)-(h), quantitative criteria have yet to be made. However, guidelines exist for normal sperm selection, such as preferences on high LIN (linearity) and small midpiece angle (the angle between the head major axis and the midpiece).

Compared to the status quo of qualitative estimation of single sperm's motility and morphology based on embryologists' empirical experience, the automation techniques provide quantitative data in nearly real time. In addition, in present clinical practice, after observing sperm motility under low magnification, it is difficult and time-consuming for a human operator to relocate the same sperm of interest identified under low magnification after switching to high magnification. The techniques presented in this paper, for the first time, enables automated, non-invasive measurement of motility and morphology parameters of the same individual sperms. With these techniques and in collaboration with the IVF community, more comprehensive criteria for quantifying and ranking the quality of single sperms can potentially be defined, a topic we are pursuing as the next step of research.

V. Conclusion

This paper presented automated non-invasive measurement of motility and morphology parameters of single sperms. For sperm motility measurement, an adapted joint probabilistic data association filter was developed to achieve simultaneous tracking of multiple sperms (tracking accuracy: 95.6%). Automated magnification switch was performed to measure the same sperm's morphology under high magnification after measuring its motility parameters under low magnification. The position of the motile sperm after magnification switch was predicted and coordinate transformation was conducted to relocate the same sperm inside the field of view after switching to high magnification, with a positioning accuracy of 5.2 μm. Total variation norm was integrated into the cost function for DIC image reconstruction. Experimental results demonstrated that the measurement errors for all morphology parameters were less than 10%.

References

[1] C. Zimmer, E. Labruyère, V. Meas-Yedid, N. Guillén, and J. C. Olivo-Marin, "Segmentation and tracking of migrating cells in videomicroscopy with parametric active contours: A tool for cell-based drug testing," *IEEE Trans. Med. Imag.*, vol. 21, no. 10, pp. 1212–1221, Oct. 2002.

[2] P. Friedl and K. Wolf, "Tumour-cell invasion and migration: Diversity and escape mechanisms," *Nature Rev. Cancer*, vol. 3, no. 5, pp. 362–374, 2003.

[3] S. Giampieri *et al.*, "Localized and reversible TGFβ signalling switches breast cancer cells from cohesive to single cell motility," *Nature Cell Biol.*, vol. 11, no. 11, pp. 1287–1296, 2009.

[4] X. Wu *et al.*, "*In vivo* and *in situ* tracking cancer chemotherapy by highly photostable NIR fluorescent theranostic prodrug," *J. Amer. Chem. Soc.*, vol. 136, no. 9, pp. 3579–3588, 2014.

[5] E. T. Donnelly, S. E. Lewis, J. A.McNally, and W. Thompson, "*In vitro* fertilization and pregnancy rates: The influence of sperm motility and morphology on IVF outcome," *Fertility Sterility*, vol. 70, no. 2, pp. 305–314, 1998.

[6] D. S. Guzick *et al.*, "Sperm morphology, motility, and concentration in fertile and infertile men," *New England J. Med.*, vol. 345, no. 19, pp. 1388–1393, 2001.

[7] P. Rubino, P. Viganò, A. Luddi, and P. Piomboni, "The ICSI procedure from past to future: A systematic review of the more controversial aspects," *Hum. Reproduction Update*, vol. 22, no. 2, pp. 194–227, 2015.

[8] A. Berkovitz *et al.*, "How to improve IVF–ICSI outcome by sperm selection," *Reproduction Biomed. Online*, vol. 12, no. 5, pp. 634–638, 2006.

[9] D. Sakkas, M. Ramalingam, N. Garrido, and C. L. Barratt, "Sperm selection in natural conception: What can we learn from mother nature to improve assisted reproduction outcomes?" *Hum. Reproduction Update*, vol. 21, no. 6, pp. 711–726, 2015.

[10] World Health Organization, *WHO Laboratory Manual for the Examination and Processing of Human Semen*. Geneva, Switzerland: WHO Press, 2010.

[11] X. P. Zhang, C. Leung, Z. Lu, N. Esfandiari, R. F. Casper, and Y. Sun, "Controlled aspiration and positioning of biological cells in a micropipette," *IEEE Trans. Biomed. Eng.*, vol. 59, no. 4, pp. 1032–1040, Apr. 2012.

[12] N. Chenouard *et al.*, "Objective comparison of particle tracking methods," *Nature Methods*, vol. 11, no. 3, pp. 281–289, Mar. 2014.

[13] L. F. Urbano, P. Masson, M. VerMilyea, and M. Kam, "Automatic tracking and motility analysis of human sperm in time-lapse images," *IEEE Trans. Med. Imag.*, vol. 36, no. 3, pp. 792–801, Mar. 2017.

[14] V. Chang, J. M. Saavedra, V. Castañeda, L. Sarabia, N. Hitschfeld, and S. Härtel, "Gold-standard and improved framework for sperm head segmentation," *Comput. Methods Programs Bio.*, vol. 117, no. 2, pp. 225–237, 2014.

[15] A. Bijar, A. P. Benavent, M. Mikaeili, and R. Khayati, "Fully automatic identification and discrimination of sperm's parts in microscopic images of stained human semen smear," *J. Biomed. Sci. Eng.*, vol. 5, no. 7, pp. 384–395, 2012.

[16] B. Obara, M. A. Roberts, J. P. Armitage, and V. Grau, "Bacterial cell identification in differential interference contrast microscopy images," *BMC Bioinf.*, vol. 14, no. 1, p. 134, 2013.

[17] B. Bartoov, A. Berkovitz, and F. Eltes, "Selection of spermatozoa with normal nuclei to improve the pregnancy rate with intracytoplasmic sperm injection," *New England J. Med.*, vol. 345, no. 14, pp. 1067–1068, 2001.

[18] A. De Vos, N. P. Polyzos, G. Verheyen, and H. Tournaye, "Intracytoplasmic morphologically selected sperm injection (IMSI): A critical and evidence-based review," *Basic Clin. Androl.*, vol. 23, no. 1, p. 10, 2013.

[19] F. Kagalwala and T. Kanade, "Reconstructing specimens using DIC microscope images," *IEEE Trans. Syst., Man, Cybern. B. Cybern.*, vol. 33, no. 5, pp. 728–737, Oct. 2003.

[20] F. Boitrelle *et al.*, "The nature of human sperm head vacuoles: A systematic literature review," *Basic Clin. Androl.*, vol. 23, no. 1, pp. 3–11, 2013.

[21] P. Vanderzwalmen *et al.*, "Blastocyst development after sperm selection at high magnification is associated with size and number of nuclear vacuoles," *Reproductive Biomed. Online*, vol. 17, no. 5, pp. 617–627, 2008.

[22] F. Boitrelle *et al.*, "High-magnification selection of spermatozoa prior to oocyte injection: Confirmed and potential indications," *Reproductive Biomed. Online*, vol. 28, no. 1, pp. 6–13, 2014.

[23] B. Tamadazte, N. L.-F. Piat, and S. Dembélé, "Robotic micromanipulation and microassembly using monoview and multiscale visual servoing," *IEEE/ASME Trans. Mechatronics*, vol. 16, no. 2, pp. 277–287, Apr. 2011.

[24] K. O. Arras, S. Grzonka, M. Luber, and W. Burgard, "Efficient people tracking in laser range data using a multi-hypothesis leg-tracker with adaptive occlusion probabilities," in *Proc. IEEE Int. Conf. Robot. Autom.*, May 2008, pp. 1710–1715.

[25] Y. Bar-Shalom, F. Daum, and J. Huang, "The probabilistic data association filter," *IEEE Control Syst.*, vol. 29, no. 6, pp. 82–100, Dec. 2009.

[26] W. Jiang and Z. Yin, "Seeing the invisible in differential interference contrast microscopy images," *Med. Image Anal.*, vol. 34, pp. 65–81, Dec. 2016.

[27] B. Heise, A. Sonnleitner, and E. P. Klement, "DIC image reconstruction on large cell scans," *Microscopy Res. Techn.*, vol. 66, no. 6, pp. 312–320, 2005.

[28] L. I. Rudin, S. Osher, and E. Fatemi, "Nonlinear total variation based noise removal algorithms," *Phys. D, Nonlinear Phenomena*, vol. 60, nos. 1–4, pp. 259–268, 1992.

[29] Z. Yin, D. F. Ker, and T. Kanade, "Restoring DIC microscopy images from multiple shear directions," in *Proc. Int. Conf. Inf. Process Medi. Imag.*, 2011, pp. 384–397.

[30] K.-S. Chuang, H.-L. Tzeng, S. Chen, J. Wu, and T.-J. Chen, "Fuzzy c-means clustering with spatial information for image segmentation," *Comput. Med. Imag. Graph.*, vol. 30, pp. 9–15, Jan. 2006.

[31] Y. Yang, C. Zheng, and P. Lin, "Fuzzy c-means clustering algorithm with a novel penalty term for image segmentation," *Opto-Electron. Rev.*, vol. 13, no. 4, pp. 309–315, 2005.

[32] F. Ghasemian, S. A. Mirroshandel, S. Monji-Azad, M. Azarnia, and Z. Zahiri, "An efficient method for automatic morphological abnormality detection from human sperm images," *Comput. Methods Programs Biomed.*, vol. 122, no. 3, pp. 409–420, 2015.

[33] K. Bernardin and R. Stiefelhagen, "Evaluating multiple object tracking performance: The CLEAR MOT metrics," *J. Image Video Process.*, vol. 2008, pp. 1–10, Dec. 2008.

[34] W. V. Holt and K. J. W. Van Look, "Concepts in sperm heterogeneity, sperm selection and sperm competition as biological foundations for laboratory tests of semen quality," *Reproduction*, vol. 127, no. 5, pp. 527–535, 2004.

[35] World Health Organisation, *WHO Laboratory Manual for the Examination of Human Semen and Sperm-Cervical Mucus Interaction*. Cambridge, U.K.: Cambridge Univ. Press, 1999.

[36] A. A. El-Ghobashy and C. R. West, "The human sperm head: A key for successful fertilization," *J. Androl.*, vol. 24, no. 2, pp. 232–238, 2003.